Available online at www.sciencedirect.com
SCIENCE DIRECT®
Journal of Computational Physics 195 (2004) 117–142
JOURNAL OF COMPUTATIONAL PHYSICS
www.elsevier.com/locate/jcp

A moving overset grid method for interface dynamics applied to non-Newtonian Hele–Shaw flow

Petri Fast [a,*], Michael J. Shelley [b]

[a] Lawrence Livermore National Laboratory, Center for Applied Scientific Computing, P.O. Box 808, L-365 Livermore, CA 94551, USA
[b] Courant Institute of Mathematical Sciences, New York University, New York, NY 10012, USA

Received 16 May 2003; accepted 27 August 2003

Abstract

We present a novel moving overset grid scheme for the accurate and efficient long-time simulation of an air bubble displacing a non-Newtonian fluid in the prototypical thin film device, the Hele–Shaw cell. We use a two-dimensional generalization of Darcy's law that accounts for shear thinning of a non-Newtonian fluid. In the limit of weak shear thinning, the pressure is found from a ladder of two linear elliptic boundary value problems, each to be solved in the whole fluid domain. A moving body fitted grid is used to resolve the flow near the interface, while most of the fluid domain is covered with a fixed Cartesian grid. Our use of body-conforming grids reduces grid anisotropy effects and allows the accurate modeling of boundary conditions.
© 2003 Elsevier Inc. All rights reserved.

1. Introduction

Consider two parallel glass plates separated by a thin layer of fluid and with a small hole drilled at the center of the top plate (Fig. 1). As air is pumped slowly through the hole into the gap an air bubble expands and displaces the fluid. The initially circular interface separating the expanding air bubble from the fluid will start to develop structure. This is called the Saffman–Taylor instability [34]. Fingers of air will advance into the fluid while other parts of the interface cease to move, forming narrow inlets of fluid referred to as fjords [30]. The "viscous fingers" in a Newtonian fluid have a tendency to split at their tips and so form new fingers, eventually resulting in a densely branched interfacial structure. This morphology has also been observed in careful numerical simulations [21].

The Saffman–Taylor instability is a prototypical free-boundary problem that shares many of the difficulties often encountered in simulations of dynamic boundaries in fluids: the incompressibility condition leads to an elliptic (Laplace) equation for the pressure that must be solved in the time-dependent domain

* Corresponding author. Tel.: +1-925-424-2649.
E-mail address: fast1@llnl.gov (P. Fast).

0021-9991/$ - see front matter © 2003 Elsevier Inc. All rights reserved.
doi:10.1016/j.jcp.2003.08.034

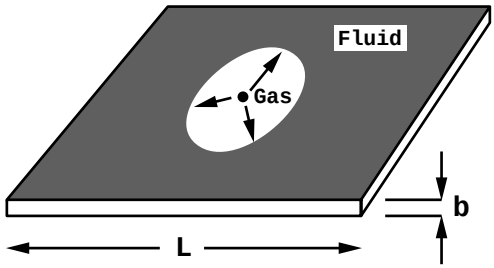

Fig. 1. The Hele–Shaw cell is the prototypical thin gap flow device.

created by the free boundary dynamics, and the capillary forces at the interface make the time evolution problem very stiff. There is also a close analogy between the Saffman–Taylor instability of driven Newtonian fluid with quasi-static solidification (and the Mullins–Sekerka instability [26]), as well as many other physical problems, such as electrochemical deposition [5]. Hence, this is an excellent test case for numerical methods used to simulate the dynamics of moving interfaces.

In this paper, we develop a numerical method for studying the Saffman–Taylor instability when the fluid being displaced by air is non-Newtonian – in particular, we focus on "shear-thinning" fluids which are characterized by a viscosity that is a decreasing function of the local shear-rate [16]. Experiments performed with complex liquids such as liquid crystals [7,8], polymer solutions and melts [39,40], clays [12], and foams [29], have shown that viscous fingers displacing a shear-thinning non-Newtonian fluid can have a dramatically different character than in Newtonian fluids: instead of repeated tip-splitting of the viscous fingers, one sees thin finger-like structures with reduced tip-splittings. This apparent stabilization of the tip leads to a fingering pattern for the shear-thinning case that is often more dendritic in appearance, and with significant side-branching. These features are absent in the case of Newtonian flow.

Kondic et al. [24,25] developed a non-Newtonian Darcy's law that describes Hele–Shaw flow in shear-thinning fluids governed by a generalized Navier–Stokes equation [4]. Unlike the Newtonian case, there is no reduction of the problem through a boundary integral treatment, and the pressure must be determined everywhere in the flow domain. Kondic et al. [25] and Fast, Kondic, Shelley and Palffy-Muhoray [16] performed fully non-linear simulations of the non-Newtonian Saffman–Taylor instability using a Lagrangian grid method with an imposed fourfold symmetry and a finite difference discretization of the interfacial quantities and the fluid equations. Their computations were limited to the early stages of the Saffman–Taylor instability due to mesh distortion. However, their simulations did suggest that shear-thinning can cause reduced tip-splitting, and yield viscous fingering patterns with strong resemblance to interfacial motifs from solidification. Fast et al. [16] showed, among other things, that the non-Newtonian Darcy's law could be derived for a broad class of viscoelastic fluid equations, under appropriate constraints on the Weissenberg number.

The purpose of this paper is to develop an accurate and efficient numerical method for studying viscous fingering in weakly shear-thinning fluids and that allows long time simulation without imposed symmetries. Level set or immersed boundary methods are also good candidates for the boundary dynamics, but can suffer from anisotropy errors arising from the underlying grid [23], while Lagrangian grid methods [16,25] can suffer from grid distortion. We strike a balance between these two extremes by using the moving overset grid method.

1.1. The moving overset grid method

We introduce the *moving overset grid method* which is the key new result of this paper. An overset grid is a collection of structured component grids, and the interpolation conditions used to connect the component

grids. In our computations, we use three component grids: a Cartesian background grid, an annular outermost grid, and a thin body-conforming grid near the interface (Fig. 2).

To achieve a highly accurate surface representation we track the free boundary explicitly, and use a body fitted grid next to the moving boundary (Fig. 2). Fig. 3 shows the viscosity in a computation of the non-Newtonian Saffman–Taylor instability using our moving overset grid method. As the boundary moves and deforms, we adapt the shape of the body fitted grid to follow the shape and motion of the moving fluid interface (Fig. 4). This grid structure has the advantage that boundaries are represented explicitly and hence boundary conditions can be modeled accurately. The method allows long time simulation of complex viscous fingering patterns in non-Newtonian Hele–Shaw flow as seen in Figs. 3 and 4, and in Section 4. Overset grids have been used previously in computations with rigid moving objects, but not for studying deforming time-dependent boundaries (see e.g. [28] and the references therein).

In Section 3, we present the details of the numerical method, which couples an overset grid discretization of the fluid equations to a Fourier based representation of the dynamic interface. The fluid velocity is obtained from a set of Poisson problems for the pressure, and these equations are solved using second-order accurate curvilinear grid finite differences and overset grids. All interfacial quantities, such as the curvature, are evaluated using Fourier-space methods. We find that this leads to greater accuracy in resolving the small length-scales of the interfacial dynamics. The method is formally second-order accurate. In Section 4, we present several numerical experiments of a gas bubble displacing a fluid in a Hele–Shaw cell, and study the resulting interfacial instability.

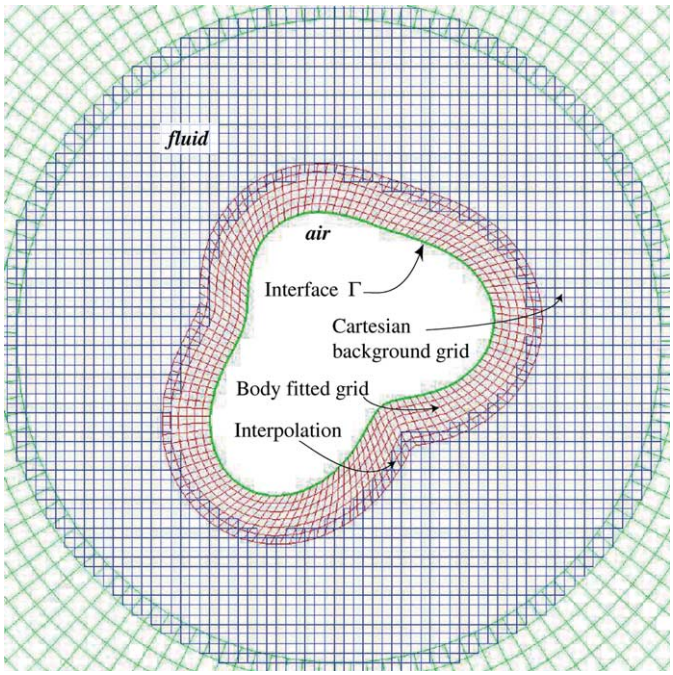

Fig. 2. A close-up of an overset grid used to discretize the fluid domain: an inner grid conforms to the interface, while a square Cartesian grid is used to cover the majority of the computational domain. An annular grid is used near the outflow. These overlapping components are joined by interpolation conditions.

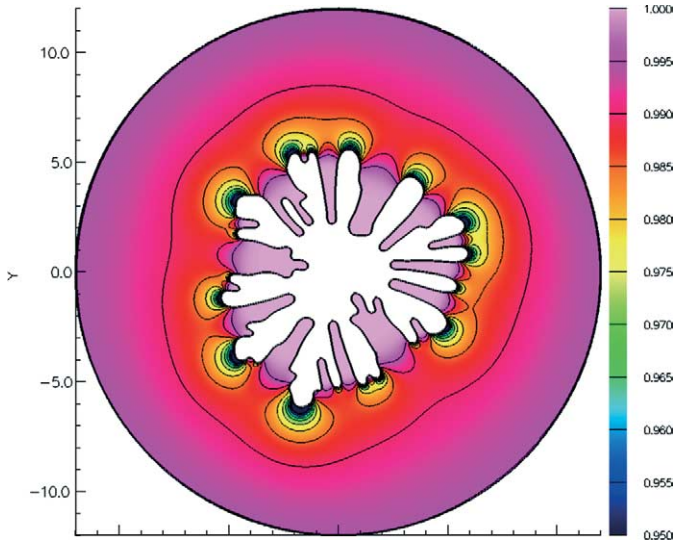

Fig. 3. The viscosity field at $t = 3.4$ in a moving overset grid computation of the Saffman–Taylor instability in a weakly non-Newtonian fluid ($We = 0.55$, $\alpha = 0.15$, $Ca = 500$). The viscosity at the tips is lowered by the shear-thinning effect.

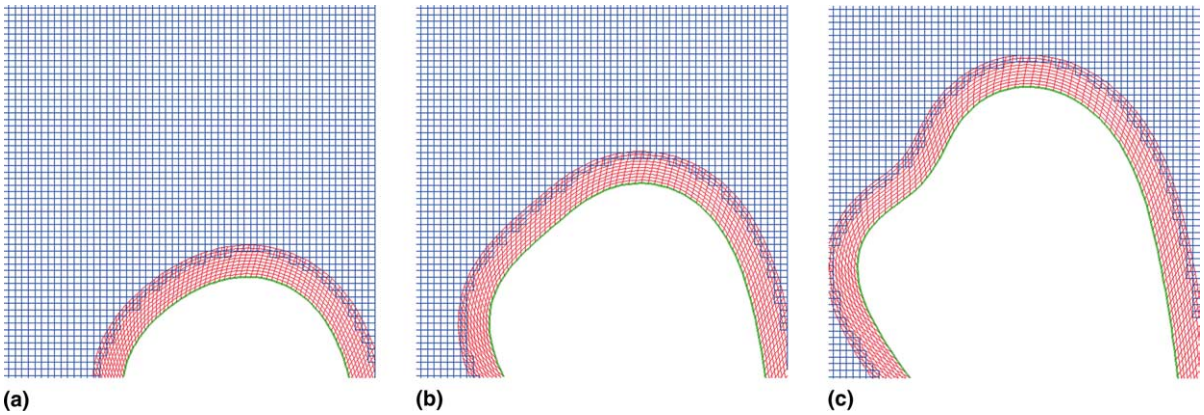

Fig. 4. A sequence showing a close up of the moving overset grids used to compute the interfacial shape in Fig. 3, at (a) $t = 1.56$, (b) $t = 1.76$, (c) $t = 1.96$.

2. Non-Newtonian Hele–Shaw flow

We now summarize two-dimensional equations of motion for non-Newtonian Hele–Shaw flow. Full details of the model are available in Fast et al. [16]. In Section 3, we develop a numerical method for the resulting two-dimensional system of Eqs. (3)–(10) that models non-Newtonian viscous fingering.

A typical control parameter for a viscoelastic fluid is the non-dimensional shear-rate

$$We = \frac{\tau U}{b} \tag{1}$$

called the Weissenberg number [4]. Here τ is a characteristic response time of the fluid, U is a characteristic velocity of the flow and b is the gap width. $We = 0$ gives a Newtonian flow, while for $We > 0$ the flow is non-Newtonian. The non-Newtonian Darcy's law derived in [16] is

$$\mathbf{u} = -\frac{\nabla p}{\bar{\mu}(We^2|\nabla p|^2)}, \quad \nabla \cdot \mathbf{u} = 0. \tag{2}$$

Here $\mathbf{u}$ is the gap averaged longitudinal velocity, p is the fluid pressure, and $\bar{\mu}(We^2|\nabla p|^2;\alpha)$ is the gap-averaged effective viscosity, depending on the squared pressure gradient, and on a shear-thinning parameter α. When $\alpha = 1$, the fluid is Newtonian with a constant viscosity, and when $\alpha < 1$, the viscosity decreases with an increasing shear-rate. The effective viscosity, plotted in Fig. 5, is derived from the physical viscosity μ. An explicit form for $\bar{\mu}$, and some restrictions on α, are given in [16, Appendix A].

2.1. Weakly non-Newtonian model

We consider a weakly shear-thinning Hele–Shaw flow, $We \ll 1$. The weakly non-Newtonian model is obtained by expanding the velocity $\mathbf{u}$, pressure p, and Eq. (2) in a small $We^2 \ll 1$ limit

$$\mathbf{u} = \mathbf{u}_0 + We^2\mathbf{u}_1 + \mathrm{O}(We^4), \tag{3}$$

$$p = p_0 + We^2 p_1 + \mathrm{O}(We^4), \tag{4}$$

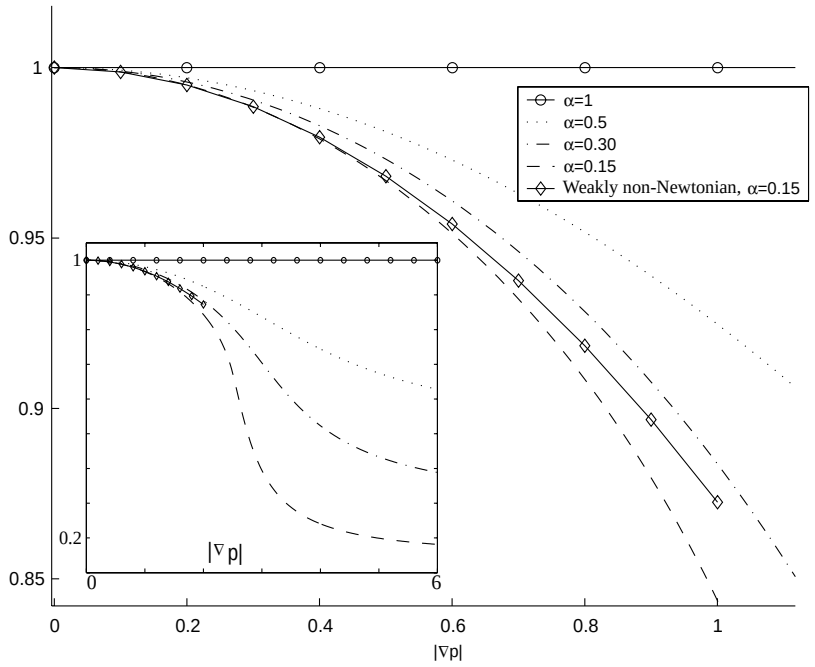

Fig. 5. The effective viscosity $\bar{\mu}$ for some typical values of α with $We = 1$ compared to the weakly non-Newtonian approximation for small $|\nabla p|$. The inset shows the viscosity for larger values of the local shear-rate $|\nabla p|$, whereas the large plot is a close-up of the region where the weakly non-Newtonian approximation is valid. Changes in We rescale the abscissa.

$$\mathbf{u}_0 = -\nabla p_0, \quad \nabla \cdot \mathbf{u}_0 = 0, \tag{5}$$

$$\mathbf{u}_1 = -\nabla p_1 - \tilde{\alpha}|\nabla p_0|^2 \nabla p_0, \quad \nabla \cdot \mathbf{u}_1 = 0, \tag{6}$$

where $\tilde{\alpha} = 3(1-\alpha)/20$, and the viscosity has been approximated by

$$\bar{\mu}(We^2|\nabla p|^2) = 1 - \frac{3(1-\alpha)}{20} We^2 |\nabla p|^2 + \mathrm{O}(We^4). \tag{7}$$

2.2. Free surface boundary conditions

The pressure satisfies a jump condition at the interface separating the fluid and the gas. We use the Young–Laplace condition

$$[p]_\Gamma = -Ca^{-1}\kappa \tag{8}$$

for comparison with earlier computations [16,21,25]. Here the modified capillary number is $Ca = 12\varepsilon^{-2}\mu_0 U/\gamma$, μ_0 is the zero-shear rate viscosity, U is a characteristic lateral velocity, and γ is the surface tension of the fluid. More accurate boundary conditions have been derived for Newtonian fluids [20], and for non-Newtonian fluids [13,32].

The interface Γ moves with the local fluid velocity according to the kinematic condition

$$\frac{\partial \mathbf{x}}{\partial t}(\beta, t) = \mathbf{u}|_{\mathbf{x}(\beta,t)}, \tag{9}$$

where β is a Lagrangian parameter.

2.3. Outflow conditions

We consider flow in circular Hele–Shaw cell with radius R_{out}. At the outer edge of the cell ($r = R_{\mathrm{out}}$), we impose on the pressure $p = p_0 + We^2 p_1$ a specified mass flux $S_t(t)$ through the outflow condition

$$\hat{\mathbf{r}} \cdot \mathbf{u} = \frac{S_t}{2\pi R_{\mathrm{out}}}, \tag{10}$$

where $\hat{\mathbf{r}}$ is a unit vector in the radial direction, and $S(t) = 2\pi(1+t)$. In terms of the pressure, the outflow boundary condition at $r = R_{\mathrm{out}}$ is

$$\frac{\partial p_0}{\partial r} = -\frac{S_t}{2\pi R_{\mathrm{out}}} \quad \text{and} \quad \frac{\partial p_1}{\partial r} = -\frac{3(1-\alpha)}{20}|\nabla p_0|^2 \frac{\partial p_0}{\partial r}.$$

This leads to the bubble area growing at a specified rate.

3. Numerical scheme

In this section, we discuss the numerical scheme for simulating the evolution problem (3)–(10) when a gas bubble expands into a weakly non-Newtonian fluid. The scheme is summarized as follows:

Step 1. Generate an overset grid and discretization: Given the boundary $\Gamma(t_n)$ at time t_n, generate an overset grid in the fluid domain exterior to $\Gamma(t_n)$. Discretize the Poisson equations (11)–(14) for the pressure fields p_0 and p_1.

Step 2(a). Solve the Newtonian pressure equation:

$$\Delta p_0 = 0 \quad \text{in } \Omega, \tag{11}$$

$$p_0|_\Gamma = -Ca^{-1}\kappa, \qquad \frac{\partial p_0}{\partial r}(\mathbf{x},t) = -\frac{S_t}{2\pi|\mathbf{x}|} \quad \text{at } |\mathbf{x}| = R_{\text{out}}. \tag{12}$$

Step 2(b). Solve the non-Newtonian pressure correction equation:

$$\Delta p_1 = -\frac{3(1-\alpha)}{20}\nabla\cdot\left(|\nabla p_0|^2\nabla p_0\right) \quad \text{in } \Omega, \tag{13}$$

$$p_1|_\Gamma = 0, \quad \frac{\partial p_1}{\partial r}(\mathbf{x},t) = -\frac{3(1-\alpha)}{20}|\nabla p_0|^2\frac{\partial p_0}{\partial r}, \quad \text{at } |\mathbf{x}| = R_{\text{out}}. \tag{14}$$

Step 3. Evaluate the velocity on Γ using Darcy's law:

$$\mathbf{u}_0 = -\nabla p_0, \quad \mathbf{u}_1 = -\nabla p_1 - \frac{3(1-\alpha)}{20}|\nabla p_0|^2\nabla p_0,$$
$$\mathbf{u} = \mathbf{u}_0 + We^2\mathbf{u}_1.$$

Step 4. Evolve the interface Γ using the kinematic condition:

$$\frac{\partial \mathbf{x}}{\partial t}(\beta,t) = U(\beta,t)\mathbf{n}(\beta,t) + T(\beta,t)\mathbf{s}(\beta,t), \tag{15}$$

where $\mathbf{s}$ is the tangent vector to Γ, $\mathbf{n}$ is the normal vector, $U(\beta,t) = \mathbf{n}\cdot\mathbf{u}(\mathbf{x}(\beta,t))$ is the normal velocity from Darcy's law, and $T(\beta,t)$ is an arbitrary tangential velocity to be set in the numerical scheme.

We now discuss the solution of each of the Steps 1–4 in detail.

Remarks. (1) The purely Newtonian case can be solved much more efficiently using boundary integral methods (see for example [21]). In the non-Newtonian case here, the pressure field satisfies a Poisson problem so boundary integral methods cannot be used.

(2) This problem shares many of the difficulties of simulating the strongly shear-thinning model (Eqs. (2), (8)–(10)). In both cases, one must at each timestep generate the overset grid discretization of the fluid domain, and solve large linear systems arising from discretizing elliptic equations. In the non-Newtonian case, the pressure satisfies the non-linear boundary value problem (Eqs. (2), (8) and (10)), which must be solved for in the whole moving domain. Since the problem is driven by the curvature of the boundaries, high spatial resolution is required. Further, there is a severe stability constraint on the temporal stepsize. In the present paper, we focus on capturing the motion of the interface in a long time simulation of weakly shear-thinning flow. The general case of strongly shear-thinning flow is left for future work.

3.1. Overset grid generation and discretization

As the free interface Γ moves, the body fitted grid and the overset grid is regenerated at each timestep (Sections 3.1.1 and 3.1.2). Given the overset grid, we discretize the pressure equations using curvilinear grid finite-differences. (Section 3.1.3).

3.1.1. Moving overset grid generation

Our implementation uses the grid generation capabilities in the Overture C++ framework [6], which is used to produce the overset grid at each time step, and the second-order discretization of the Laplace

operator in the time-dependent fluid region. The algorithm used in Overture is based upon the original CMPGRD algorithm [10] with major changes to improve robustness [19]. Typically, the amount of computational time spent for overset grid generation at each time step is insignificant in comparison to the pressure solve. For a detailed description of the overset grid generator, see [19].

3.1.2. Body fitted grid generation

The body-conforming grid is generated by marching outward from the interface Γ. The grid corresponds to a uniform grid discretization of the the mapping

$$\mathbf{x}(\xi,\eta), \quad 0 \leqslant \xi \leqslant 1, \;\; 0 \leqslant \eta \leqslant 2\pi,$$

where $\mathbf{x}(0,\eta)$ is the interface Γ, and the lines $\eta \equiv$ Const. are rays extending outwards from the bubble in the normal direction (Fig. 6). Hyperbolic grid generation [9] is often used to produce such grids around complicated geometries. In the present case, a simpler approach can be used. We generate the body fitted grid by marching

$$\mathbf{x}_\xi(\xi,\eta) = -(1 - C\kappa(\xi,\eta))\mathbf{n}(\xi,\eta) + T(\xi,\eta)\mathbf{s}(\xi,\eta) \tag{16}$$

in the pseudo-time ξ starting from the interface Γ at $\xi = 0$. Here C is a small constant, κ is the curvature of a gridline along $\xi \equiv$ Const., $\mathbf{n}(\xi,\eta)$ is the normal vector, and $\mathbf{s}(\xi,\eta)$ is the tangent vector to the curve $\mathbf{x}(\xi,\eta)$, for $\xi \equiv$ Const. The normal velocity $U = -(1 - C\kappa(\xi,\eta))$ gives Eq. (16) a diffusive character [21], and has been used previously for grid generation [35]. The tangential velocity $T(\xi,\eta)$ is chosen to maintain equi-spacing in the η-direction (see [21] for details). To generate the body fitted grid on each time-step, we solve Eq. (16) using a time evolution method similar to the one used in Section 3.3 (with $t = \xi$, $\beta = \eta$, see Appendix B).

3.1.3. Finite difference discretization

An overset grid consists of structured, curvilinear component grids each defined by a mapping $\mathbf{x}(\mathbf{r},t) = \mathbf{G}(\mathbf{r},t)$, where $\mathbf{r} = (r,s)$, and $0 \leqslant r,s \leqslant 1$.

The derivatives of a function f with respect to the physical variables (x,y) are transformed to derivatives in the computational variables (r,s) through the chain-rule

$$\frac{\partial f}{\partial x} = r_x \frac{\partial \tilde{f}}{\partial r} + s_x \frac{\partial \tilde{f}}{\partial s}, \tag{17}$$

$$\frac{\partial f}{\partial y} = r_y \frac{\partial \tilde{f}}{\partial r} + s_y \frac{\partial \tilde{f}}{\partial s}, \tag{18}$$

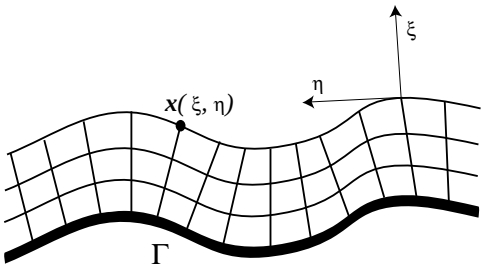

Fig. 6. The body fitted grid is generated by marching outward from the interface Γ (see text).

$$\nabla^2 f = (r_x^2 + r_y^2)\frac{\partial^2 \tilde{f}}{\partial r^2} + 2(r_x s_x + r_y s_y)\frac{\partial^2 \tilde{f}}{\partial r \partial s} + (s_x^2 + s_y^2)\frac{\partial^2 \tilde{f}}{\partial s^2} + \left(\nabla^2 r\right)\frac{\partial \tilde{f}}{\partial r} + \left(\nabla^2 s\right)\frac{\partial \tilde{f}}{\partial s}, \tag{19}$$

where $\tilde{f}(r,s) = f(x(r,s), y(r,s))$, and $\nabla^2 u = u_{xx} + u_{yy}$. The inverse vertex derivatives $r_x, r_y, r_{xx}, r_{yy}, s_x, s_y, s_{xx}$, and s_{yy} are computed from the mapping $\mathbf{G}$ that defines the component grid. The mapping method for finite-difference discretization is obtained by discretizing the derivatives (17)–(19) in the computational variables (r,s). We introduce a discretization of

$$r_i = i\Delta r \quad \text{and} \quad s_j = j\Delta s,$$

where $0 \leqslant i \leqslant N_r$, $\Delta r = 1/N_r$, $0 \leqslant j \leqslant N_s$, and $\Delta s = 1/N_s$. A discretized component grid is then given by $\mathbf{x}_{i,j} = \mathbf{G}(r_i, s_j)$ where $0 \leqslant i \leqslant N_r$, $0 \leqslant j \leqslant N_s$.

We define the basic difference operators in the s direction by

$$D_+^s f_{i,j} = \frac{f_{i,j+1} - f_{i,j}}{\Delta s}, \quad D_-^s f_{i,j} = \frac{f_{i,j} - f_{i,j-1}}{\Delta s}, \quad D_0^s f_{i,j} = \frac{f_{i,j+1} - f_{i,j-1}}{2\Delta s}. \tag{20}$$

Second-order accurate centered approximations to the basic derivative operators are given by

$$\frac{\partial f}{\partial s}(\mathbf{r}_{i,j}) = D_0^s f_{i,j} + \mathcal{O}(\Delta s^2), \tag{21}$$

$$\frac{\partial^2 f}{\partial s^2}(\mathbf{r}_{i,j}) = D_+^s D_-^s f_{i,j} + \mathcal{O}(\Delta s^2). \tag{22}$$

Derivatives in the r direction are defined analogously. The discretized inverse vertex derivatives are re-computed from the mapping $\mathbf{G}$ when the overset grid is regenerated.

In the physical variables (x,y), we obtain second-order accurate discrete approximations to the derivatives (17)–(19)

$$\frac{\partial f}{\partial x}(\mathbf{x}_{i,j}) \approx r_x D_0^r f + s_x D_0^s f, \tag{23}$$

$$\frac{\partial f}{\partial y}(\mathbf{x}_{i,j}) \approx r_y D_0^r f + s_y D_0^s f, \tag{24}$$

$$\begin{aligned}\nabla^2 f(\mathbf{x}_{i,j}) \approx\ & (r_x^2 + r_y^2) D_+^r D_-^r f + (s_x^2 + s_y^2) D_+^s D_-^s f \\ & + 2(r_x s_x + r_y s_y) D_0^r D_0^s f + (r_{xx} + r_{yy}) D_0^r f + (s_{xx} + s_{yy}) D_0^s f,\end{aligned} \tag{25}$$

where the right-hand side is evaluated at index (i,j). The finite difference approximation to each of the Poisson problems for the pressure (11)–(14) is assembled in a sparse matrix and passed to a linear solver. The interpolation and boundary conditions generate additional linear constraints which are placed in the sparse matrix (see [10] for further details).

3.2. Solving the pressure equations

The discretization of the pressure Eqs. (11)–(13) in our simulations leads to a sparse linear system of equations with 250,000–630,000 unknowns. The numerical solution of the resulting non-symmetric system of linear equations is the major computational task in our numerical method.

To solve the linear systems arising from the pressure equations, we use an iterative method with an incomplete LU (ILU) preconditioner (see [33] and the references therein for a detailed discussion of the linear solvers and preconditioners). Our implementation combines several well-known methods to achieve significant performance improvement over the approaches used thus far. Earlier work with incompressible flow on overset grids [18] used the generalized minimal residual method (GMRES) with an ILU(0) preconditioner (no fill-in), which performs rather poorly; sparse direct factorization methods are much faster for moderately sized time-stepping problems on fixed grids [10,18]. However, the cost of such a method in a moving grid computation would be prohibitive.

We have found that an effective preconditioner for a Krylov space iterative method in the present case can be formulated as follows:

(1) Rescale the the matrix so that each row has norm 1.
(2) Perform a reverse Cuthill–McKee (RCM) reordering of the matrix.
(3) Build an ILU(k) preconditioner with fill-in ($k > 0$, we use typically $k = 10$).

The interpolation equations in the overset grid discretization make the sparsity pattern of the matrix non-symmetric and irregular. This increases the fill-in of ILU factorization methods. The RCM reordering reduces the bandwidth of the matrix, which results in a smaller ILU(k) factorization.

We use the stabilized bi-conjugate gradient method (BICG-STAB) with the preconditioner described above to solve the pressure equations. The implementation [15] is based on the linear solver component in PETSc [2] which we have interfaced to the Overture framework.

Table 1 compares the performance of several approaches. We consider a test case for the linear solver with 2048 points at the interface, 438,644 discretization points in the overset grid, and 1,509,621 non-zeros in the sparse matrix. We list in Table 1 the number of iterations (Its.) required to reach a residual of 10^{-8}, the time to form the preconditioner (Precond.), the time taken by the linear solver (solve), and their sum (total = precond. + solve). All timings are given in seconds, and were measured on a single 250 MHz MIPS R10000 processor of an SGI Origin 2000. The computations in Section 4.2 use BiCG-Stab with ILU(10), which is almost 10 times faster than GMRES(30) with ILU(0).

The pressure solve remains the most expensive part of the method described in this paper. Multigrid methods offer an even more efficient approach to solving elliptic (Poisson) equations in overset grid flow simulations, and will be considered in future work (Henshaw, private communication).

3.3. Interface evolution

In this Subsection we discuss the numerical scheme for evolving the interface according to the kinematic boundary condition (9).

3.3.1. Motivation for reformulating the interface equations

While it would be possible to discretize the kinematic boundary condition (9) explicitly in time, it is advantageous to reformulate the problem to exploit the special structure of Eqs. (3)–(10) for the following reasons: (1) Linear stability analysis (Section 4.1.1) suggests an explicit time stepping scheme would suffer

Table 1
Comparing the performance of different approaches to solving a Poisson problem on an overlapping grid (see text)

Method	Its.	Precond.	Solve	Total
GMRES(30) + ILU(0)	755	1.2	879.0	880.2
BiCG-Stab + RCM + ILU(5)	60	6.6	125.8	132.4
BiCG-Stab + RCM + ILU(10)	36	12.6	78.5	91.1
BiCG-Stab + RCM + ILU(20)	18	36.9	59.3	96.2

from a severe restriction of the form $\Delta t \leqslant C \min |\Delta s|^3$, where $\min |\Delta s|$ is the minimum spacing between points along the discretized interface. (2) The flow is driven by the curvature κ of the the interface, and so a high-order accurate approximation to interfacial derivatives is desirable. (3) The interface is periodic, so Fourier-spectral methods are efficient and highly accurate. (4) In the case of Newtonian viscous fingering ($We = 0$), the *small scale decomposition* of Hou, Lowengrub and Shelley [21] and an equal-arclength discretization reduces the stability restriction to $\Delta t \leqslant C|\Delta s|$ where Δs is a *uniform* spacing of points along the interface, and C is a positive constant.

We use the small-scale decomposition for the Newtonian case [21] to reduce the stiffness of the time-stepping scheme also in the case of weakly non-Newtonian viscous fingering. A similar approach was used by Almgren et al. [1] to reduce the stiffness of a boundary integral scheme for Newtonian viscous fingering with an anisotropic surface tension.

3.3.2. Evolution equations reformulated in a θ–L frame

The kinematic boundary condition (15) is rewritten with new dependent variables: we define a tangent-angle $\theta(\beta, t)$ and arclength derivative $s_\beta(\beta, t)$ through

$$x_\beta(\beta, t) = s_\beta(\beta, t) \cos \theta(\beta, t), \tag{26}$$

$$y_\beta(\beta, t) = s_\beta(\beta, t) \sin \theta(\beta, t), \tag{27}$$

$$s_\beta = \sqrt{x_\beta^2 + y_\beta^2}, \tag{28}$$

and use θ and s_β instead of $x(\beta, t)$ and $y(\beta, t)$ to evolve the interface shape Γ. A special choice of the tangential velocity T (Eq. (31) below) keeps the parametrization of Γ in an equal arclength frame where the arclength derivative $s_\beta = L(t)/2\pi$ is constant in β, with $L(t)$ the length of the boundary Γ at time t.

The kinematic boundary condition (15) is transformed to the tangent angle-length frame as (Appendix A)

$$L_t = -\int_0^{2\pi} U\theta_\beta \, \mathrm{d}\beta'. \tag{29}$$

$$\theta_t = \frac{2\pi}{L(t)}(U_\beta + T\theta_\beta), \tag{30}$$

$$T(\beta, t) = T(0, t) + \int_0^\beta \theta_\beta U \, \mathrm{d}\beta' - \frac{\beta}{2\pi}\int_0^{2\pi} \theta_\beta U \, \mathrm{d}\beta'. \tag{31}$$

3.3.3. An integrating factor form using the small-scale decomposition

A detailed analysis [21] of the integral representation of the velocity in the case of Newtonian Hele–Shaw flow reveals the dominant behavior of the normal velocity U in Eq. (30). In Fourier space, the dominant part of the normal velocity for $We = 0$ and large wavenumbers ($k \gg 1$) is [21]

$$\hat{U}(k, t) \sim \frac{\mathrm{i}}{Ca}\left|\frac{2\pi k}{L(t)}\right|^2 \mathrm{sgn}(k)\hat{\theta}(k, t).$$

We express the tangent angle-length formulation in Eq. (30) as

$$L_t(t) = -\int_0^{2\pi} U(\beta', t)\theta_\beta(\beta', t)\mathrm{d}\beta', \tag{32}$$

$$\hat{\theta}_t(k,t) = -\frac{1}{Ca}\left|\frac{2\pi k}{L(t)}\right|^3 \hat{\theta}(k,t) + \hat{F}(k,t), \tag{33}$$

where

$$\hat{F} = \frac{1}{Ca}\left|\frac{2\pi k}{L}\right|^3 \hat{\theta} + \frac{2\pi}{L}\left(\mathrm{i}k\hat{U} - \frac{2\pi}{L}\widehat{T\theta_\beta}\right). \tag{34}$$

3.3.4. Linear propagator time-discretization

An integrating factor $\exp(\psi(k,t))$ exists for Eqs. (32) and (33) if we define

$$\psi(k,t) = \int^t \frac{1}{Ca}\left(\frac{2\pi k}{L(t')}\right)^3 \mathrm{d}t'.$$

Using the integrating factor, we rewrite Eq. 33 as

$$\frac{\partial}{\partial t}(\mathrm{e}^{\psi(k,t)}\hat{\theta}(k,t)) = \mathrm{e}^{\psi(k,t)}\hat{F}(k,t). \tag{35}$$

This is the form that is discretized in time and solved numerically.

Let the 2π-periodic interface $\mathbf{x}(\beta,t)$ be parametrized by $\beta_j = j\Delta\beta$, $0 \leqslant j \leqslant N-1$, where $\Delta\beta = 1/N$. We introduce a discretized time t_n, and let L^n denote the length of the interface, $\hat{\theta}^n(k)$ denote $\hat{\theta}(k,t_n)$, and $\hat{F}^n(k)$ denote $\hat{F}(k,t_n)$ in Eq. (34) at time t_n and wavenumber k. Define the integrals

$$I_j^n = \int_0^{\beta_j} \theta_{\beta'}^n U^n \,\mathrm{d}\beta', \quad \bar{I}^n = \bar{I}_N^n = \int_0^{2\pi} \theta_\beta^n U^n \,\mathrm{d}\beta. \tag{36}$$

These quadratures are evaluated using Fourier methods. For the integrating factor, we use the trapezoidal rule and define

$$\psi^n := \frac{1}{2}\frac{1}{Ca}\left\{\left(\frac{2\pi k}{L^{n+1}}\right)^3 + \left(\frac{2\pi k}{L^n}\right)^3\right\} = \frac{1}{Ca}\int_{t_n}^{t_{n+1}}\left(\frac{2\pi k}{L(t')}\right)^3 \mathrm{d}t' + \mathcal{O}(\Delta t^3).$$

We apply the second-order accurate Adams–Bashforth scheme to the integrating factor form in Eq. (35) to obtain

$$L^{n+1} = L^n - \frac{\Delta t}{2}(3\bar{I}^n - \bar{I}^{n-1}), \tag{37}$$

$$\hat{\theta}^{n+1} = \mathrm{e}^{-\psi^n}\hat{\theta}^n + \frac{\Delta t}{2}(3\mathrm{e}^{-\psi^n}\hat{F}^n - \mathrm{e}^{-(\psi^n+\psi^{n-1})}\hat{F}^{n-1}). \tag{38}$$

The length L^{n+1} is computed first, so the integrating factor $\exp(-\psi^n)$ can be evaluated directly when computing $\hat{\theta}^{n+1}$. The pseudospectral scheme (37) and (38) is semi-implicit, but the implicit part has been solved directly using an integrating factor. The derivatives and integrals are computed in Fourier space, but products of terms are computed in real space.

4. Numerical results

In this section, we present the results of numerical experiments of a gas bubble displacing a fluid in a Hele–Shaw cell.

4.1. Validation of the implementation

4.1.1. Linear stability analysis and the Saffman–Taylor instability

We consider the linear stability of a circular bubble of radius $R(t) = 1 + t$ perturbed azimuthally as it expands into a non-Newtonian fluid in an unbounded Hele–Shaw cell. The circular interface is an exact solution to the full Eqs. (3)–(10) with velocity and pressure field given by

$$u(r,t) = \frac{S_t(t)}{2\pi r}, \quad p(r,t) = \frac{1}{Ca\,R(t)} + \frac{S_t(t)}{2\pi} \ln \frac{r}{R(t)}. \tag{39}$$

both in the Newtonian, and the weakly non-Newtonian case. The theoretical linearized growth rates of perturbations are compared to growth rates extracted from simulations.

4.1.1.1. Linear theory. Assume Γ is given by

$$\mathbf{R}(\theta,t) = R(t)(1 + \varepsilon\eta(\theta,t))\hat{\mathbf{r}}, \tag{40}$$

where $\varepsilon \ll 1$ is a small parameter, $\hat{\mathbf{r}}$ is the radial unit vector, and $\eta(\theta,t)$ is a perturbation.
Since $\eta(\theta,t)$ can be written as a Fourier series in the azimuthal angle θ, and the linearized equations are separable, we consider without loss of generality a perturbation of the form

$$\eta(\theta,t) = N(m,t)\cos m\theta, \tag{41}$$

where m is a wave number. In [16] it is shown that to leading order in ε, the instantaneous growth rate $\sigma_m = N_t/N$ is given by

$$\sigma_m = -1 + m\left(1 + \mathscr{B}\frac{m-1}{m+1}\right) + Ca^{-1}m(1-m^2)\left(1 + \mathscr{B}\frac{2m}{m+1}\right). \tag{42}$$

In this weakly non-Newtonian limit the non-Newtonian character of the fluid is contained in the single small positive parameter $\mathscr{B} = (3/20)(1-\alpha)We^2$. Fig. 7 shows the analytic linear stability curves given by Eq. (42).

The key feature of Fig. 7 is that intermediate length-scales are unstable and the small length-scales (modes with large m) are strongly damped, which leads to growth of intermediate length scale perturbations of an expanding circle. This is true generally for the Saffman–Taylor instability.

In the simulations of this paper the initial data is always unstable to the Saffman–Taylor instability: when $Ca = 250$ and $We \leqslant 0.55$, modes 2–15 are unstable and mode 9 is dominant with the largest positive growth rate; when $Ca = 500$ and $We \leqslant 0.55$, modes 2–21 are unstable, and mode 13 is dominant with the largest positive growth rate. As the radius of the circle grows, the band of unstable modes expands towards larger wavenumbers.

4.1.1.2. Comparison with simulations. We use the results of linear stability analysis as a first check of our numerical method. In our simulations, we consider perturbations of the form in Eqs. (40) and (41) with a perturbation amplitude $\varepsilon = 0.001$, and modes $m = 1,\ldots,25$. For each perturbation mode m, the full equations of motion (3)–(10) are solved for five time steps. The growth rate $\tilde{\sigma}_m = \hat{\eta}_t/\hat{\eta}$ of mode m is computed from the simulation by a Fourier transformation of the perturbation

$$\eta(\beta,t) = \mathbf{x}(\beta,t) - R(t)(\cos\beta, \sin\beta)$$

and a second-order finite difference approximation of $\hat{\eta}_t$ from the computed mode amplitude $\hat{\eta}$.

In Fig. 8 we compare the analytic linear growth rates from Eq. (42) with growth rates obtained with the full overset grid code for a non-Newtonian case with $We = 0.55$, $Ca = 250$, and $Ca = 500$. The agreement between theory and simulation is good, though for large wavenumbers, the growth rates from linear theory

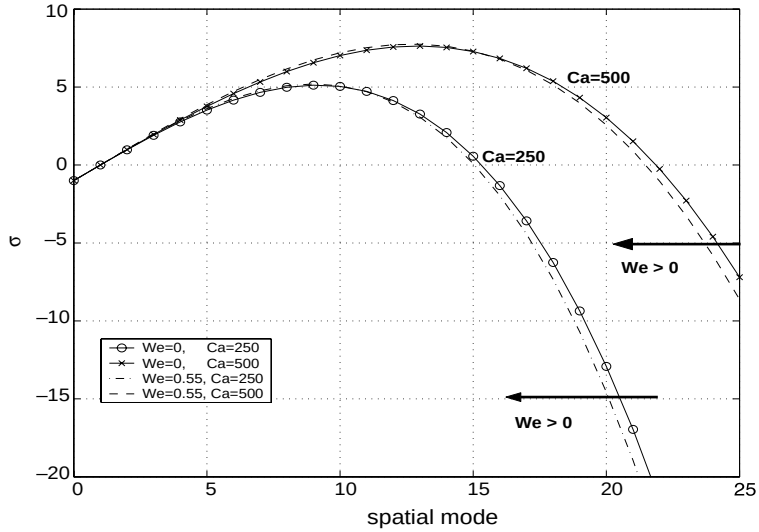

Fig. 7. Analytic results for the linearized growth rates of perturbations to a circle for different cases from Eq. (42). Note that small-scales ($m \gg 1$) are stable, and an intermediate range of lengthscales is made unstable by the Saffman–Taylor instability. In the non-Newtonian case, the band of unstable modes becomes narrower as the Weissenberg number *We* is increased.

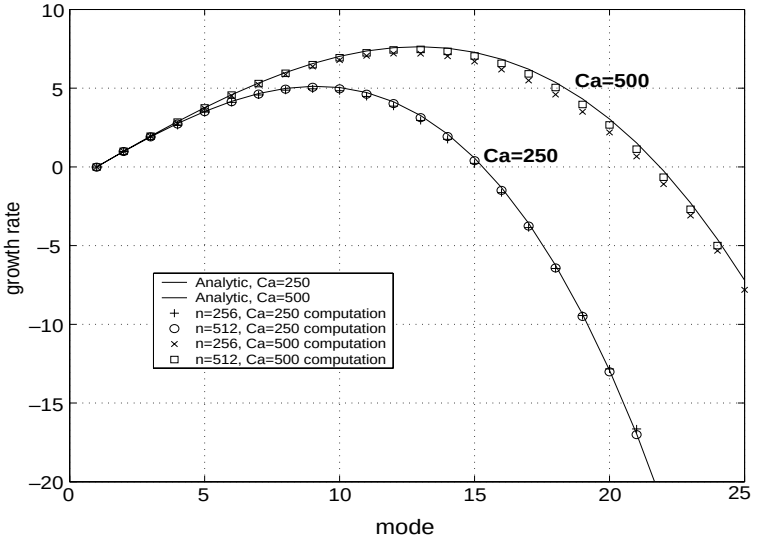

Fig. 8. Linear growth rates of perturbations in the non-Newtonian case with $We = 0.55$. Comparison of the analytic result to linear growth rates from the overset grid implementation with $Ca = 250$ or $Ca = 500$, and $n = 256$ or $n = 512$ points along the interface.

have slightly larger absolute amplitudes than the growth rates from the simulations. However, the large wavenumber behavior is strongly dissipative in the problems considered here and has little effect on the simulations as long as the wavenumbers with positive growth, and moderate damping are resolved. It is well known that finite difference schemes do not capture high frequency phenomena accurately, so it is important to resolve the length scales of interest as has been done here (see Fig. 4.-1.-3. in [17]).

Remark. It is standard practice in boundary integral simulations of interfacial instabilities to present numerically computed linearized growth rates and compare those to analytical results as has been done in this section (see [22] and references therein). However, in simulations of interfacial instabilities using finite difference and finite element methods, it is unfortunately uncommon to present those results. Since the linear instabilities are at the heart of many interfacial instabilities, it is important to discuss the fidelity of the numerical scheme in capturing this key feature of the physical problem. In this paper, the use of Fourier based methods to compute the curvature in the boundary condition (8) greatly improves the agreement with linear theory at small length scales. Further details and a theoretical model will be reported elsewhere.

4.1.2. Simulations of an expanding circle

Here, we compare the exact solution for an expanding circle to our simulations and discuss the properties of the numerical errors. We simulate a circular interface expanding into a Newtonian fluid with $Ca = 250$ and $We = 0.55$ to $t = 4$ with $\Delta t = 10^{-3}$. These parameters define a problem that is unstable to the Saffman–Taylor instability, with modes 2–15 unstable, and mode 9 having the largest initial growth rate (see Fig. 7).

To examine the nature of spatial errors, and the effect of under-resolution, we use in these simulations:

- 64 points on the interface, 60^2 points in the Cartesian background grid,
- 128 points on the interface, 120^2 points in the Cartesian background grid,
- 256 points on the interface, 240^2 points in the Cartesian background grid.

The L^∞-errors in interface position are given in Table 2, and demonstrate second-order spatial accuracy until time $t = 2$. The order of convergence drops slightly below second-order before $t = 3$ as the flow becomes under-resolved. Since the number of points on the interface is kept constant in this test, the spacing between the points grows as the interface expands. This is different from the simulations of pattern formation shown in Section 4.2 where the interfacial resolution is increased as needed. In Table 3, the point spacings are shown for an expanding circle with $N = 256$ points along the interface.

The interface is shown at several time steps $t = 0, \ldots, 4$ in Fig. 9. The solution is visually indistinguishable from the exact solution. Nonetheless, there are grid induced errors in the solution that are not visible in the plot. Fig. 10 shows the error in the radius as a function of the radial angle β for several time steps. The plots show the error for two resolutions with $N = 128$ and $N = 256$ points along the interface.

The error has a structure that suggests that the Cartesian background grid can amplify the interfacial velocity in the coordinate directions as the error in the radius has maxima at angles $\beta = 0, \pi/2, \pi, 3\pi/2$ and 2π coinciding with the directions of the x and y axes. From the linear stability analysis one would not expect mode 4 to be dominant as is seen in Fig. 10; mode 9 would be expected to grow the fastest since it has the largest growth rate. However, only perturbations that are present can be amplified by the dynamics. It seems that discretization errors give rise to a mode 4 perturbation of the circular interface which is then amplified by the Saffman–Taylor instability.

Table 2
Errors and convergence rates for a circular bubble expanding into a Newtonian fluid with $Ca = 250$

	Maximum error in interface position				
	$t = 0.5$	$t = 1$	$t = 2$	$t = 3$	$t = 4$
$N = 128$	2.9319×10^{-3}	5.2375×10^{-3}	9.5074×10^{-3}	1.3711×10^{-2}	1.8997×10^{-2}
$N = 256$	6.8139×10^{-4}	1.2264×10^{-3}	2.3069×10^{-3}	3.5213×10^{-3}	5.0478×10^{-3}
Rate	2.1053	2.0944	2.0431	1.9612	1.9120

N denotes the number of discretization points along the interface. The second-order convergence can be seen until $t = 2$. Since the length of the interface is growing in time and number of discretization points is kept fixed, the flow becomes under-resolved after $t = 2$. A slight drop in convergence rate can be seen at $t = 3$ and $t = 4$.

Table 3
The exact radius for the expanding circle

	Exact radius and grid spacing for $N = 256$				
	$t = 0.5$	$t = 1$	$t = 2$	$t = 3$	$t = 4$
$R(t)$	1.5000	2.0000	3.0000	4.0000	5.0000
Spacing along interface	0.0368	0.0491	0.0736	0.0982	0.1227

Since the interfacial resolution is kept constant in this test, the spacing of discretization points along the interface grows as the interface expands. Here, the spacings are shown for an expanding circle with $N = 256$ points along the interface. In the simulations of Section 4.2, the maximum spacing along the interface is 0.024.

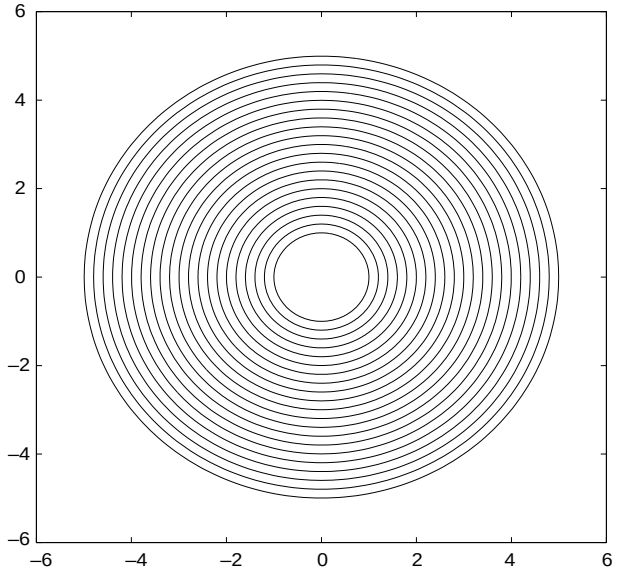

Fig. 9. A long time simulation of a circular interface expanding into a Newtonian fluid with $Ca = 250$ and $We = 0.0$ for 4000 timesteps ($T = 0, \ldots, 4$). The solution is visually indistinguishable from the exact solution. See Fig. 10 for the structure of the error in this solution.

Ultimately, the successful control of grid induced errors will be what limits the maximum temporal length of simulations of interfacial instabilities using grid based methods. Our use of body fitted grids improves the accuracy of the solution near the interface, where the velocity of the interface is computed from the pressure using Darcy's law (5) and (6). The errors here depend on the resolution as $O(h^2)$ where h is a maximum spacing in the mesh. Hence, adequate spatial resolution and high-order methods will minimize systematic discretization induced errors and allow longer simulations.

Note that in the present scheme, these grid alignment errors are not significant for the length of simulations considered here even at the lower resolutions used in Figs. 9 and 10. The asymmetric simulations discussed below begin with $N = 512$ points along the interface, and are restarted at higher resolutions to enhance accuracy with up to $N = 4096$ points along the interface at the end of a simulation.

As a further check for grid induced anisotropy, we consider an interface which is initially a circle perturbed radially by a single mode

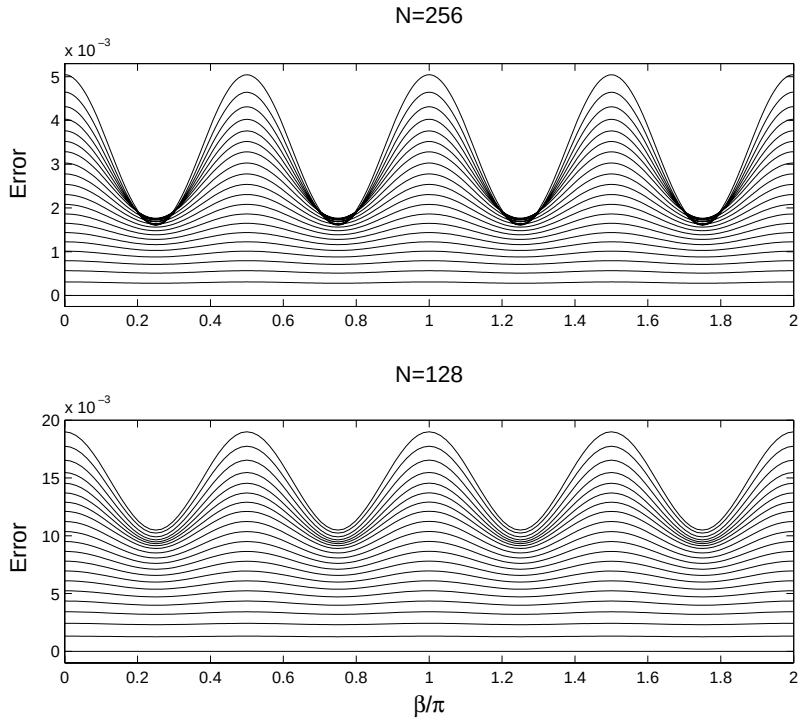

Fig. 10. Evolution of the error in the radius in simulations of an expanding circular interface (Fig. 9), for $t = 0, \ldots, 4$. The error is plotted as a function of the radial angle β for several time steps. Top: Error in the radius with $N = 256$ points on the interface with error $= 0$ at $t = 0$, and the maximum error at $t = 4$. Bottom: Error with $N = 128$ points on the interface. Note the larger errors in the coordinate directions.

$$(x_0(\beta), y_0(\beta)) = r(\beta)(\cos\beta, \sin\beta),$$

where

$$r(\beta) = 1 + 0.1\cos 4\beta.$$

For comparison, we simulate this initial data, as well as the same data rotated 22.5° counter-clockwise, expanding into a weakly non-Newtonian fluid ($We = 0.55$, $Ca = 200$) using 512 points on the interface (Fig. 11). The four-fold symmetry is not enforced by the numerical scheme, but is still preserved by the dynamics.

4.2. Simulation of the Saffman–Taylor instability

We now consider the Saffman–Taylor instability in a weakly non-Newtonian fluid whose dynamics is given by Eqs. (6)–(9). The basic elements of pattern formation for a gas bubble expanding into a Newtonian fluid in a radial Hele–Shaw cell are well understood from experiment [30], theory [3,37] and careful numerical simulation [21]. Very roughly, a perturbation of the bubble interface grows outwardly into an expanding petal. When this petal's radius of curvature exceeds the wavelength of an unstable mode, it "tip-splits" into two nascent petals, which themselves broaden and split. This repeated process yields an interface described by a population of branches and fjords, and whose evolution is characterized by strong competition among the branches, with some branches being "shielded" and retracting, and others

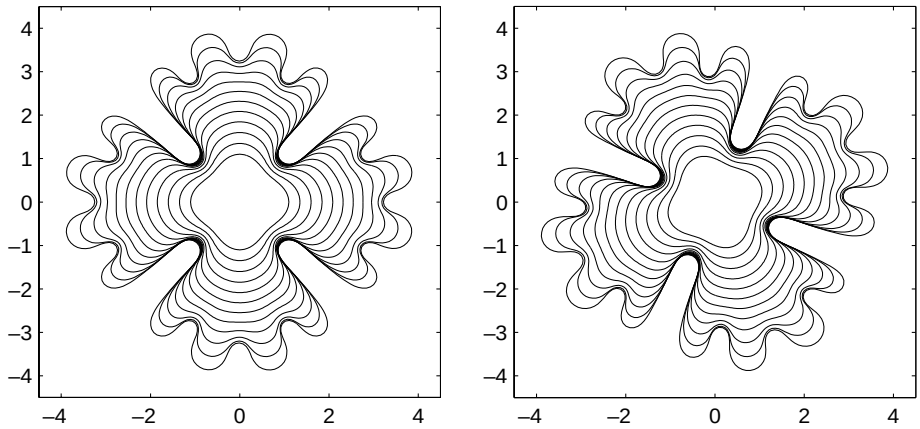

Fig. 11. Checking for grid induced anisotropy effects with $Ca = 200$, $We = 0.55$. In the leftmost figure, the initial data is a circle perturbed radially by a cosine wave of relative amplitude 0.1. In the rightmost figure, this initial data is rotated counter-clockwise by 22.5°. The fourfold symmetry in the initial data is preserved by the numerical method in both cases for $t = 0, \ldots, 2.2$. Grid orientation effects are negligible.

advancing further into the fluid. Clearly, if tip-splitting can be suppressed a much different pattern morphology will follow.

Kondic et al. [25] considered viscous fingering in a strongly shear-thinning fluid modeled by the non-Newtonian Darcy's law (2) in a radial geometry. These computations, although limited to four-fold sym-

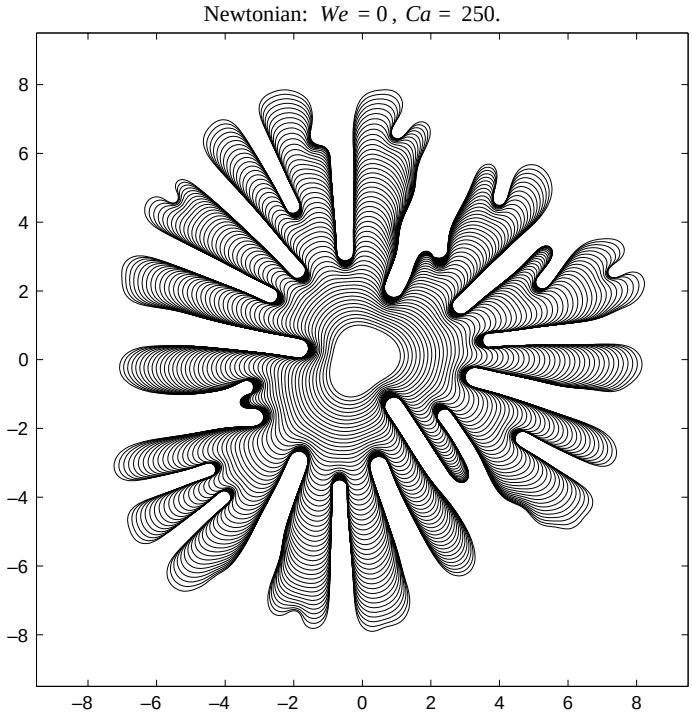

Fig. 12. Snapshots of the interface at several computational times ($t = 0, \ldots, 5.2$, in increments of 0.1) for a Newtonian case with $Ca = 250$.

metric interfaces, and to the early stages of the Saffman–Taylor instability, suggest that shear-thinning of the fluid can lead to reduced tip-splitting at small Weissenberg numbers $We < 0.50$ (see also [16]).

Poiré and Ben Amar [31] have used our generalized Darcy's law (2) to study the formation of "fractures" or "cracks" in clays and associating polymer solutions [31]. Using a shear-thinning power-law fluid, they examined the "width selection" problem for a gas finger propagating steadily down a channel in a Hele–Shaw cell. They consider the displaced fluid to be slightly shear-thinning, and show that within this asymptotic limit the selected finger width decreases to zero (i.e. a crack) as surface tension goes to zero.

In Figs. 12–15, we consider evolution of the interface at different capillary numbers, and compare Newtonian computations ($We = 0$) with weakly non-Newtonian computations ($We = 0.55$). As initial data we take

$$(x_0(\beta), y_0(\beta)) = r(\beta)(\cos\beta, \sin\beta),$$

where

$$r(\beta) = 1 + 0.1(\cos 3\beta + \sin 2\beta),$$

as in [21], and study the effects the variations in the capillary number Ca and the Weissenberg number We has on the dynamics of the evolving interface. In all cases this initial data are unstable to the Saffman–Taylor instability.

We start each simulation with 512 points on the interface, and double the resolution as needed to resolve it, up to a resolution of 4096 points. The spacing along the interface is always kept in the range $0.012 \leqslant \Delta s \leqslant 0.024$. The sizes of the grids we use to discretize the fluid domain at the different resolutions are

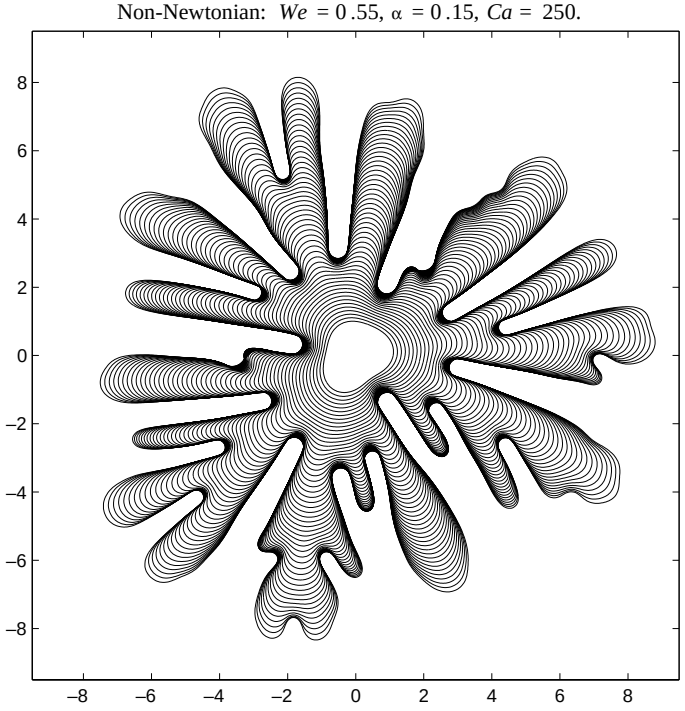

Fig. 13. The expanding air/fluid interface in a moving overset grid simulation of non-Newtonian Hele–Shaw flow at $Ca = 250$, $We = 0.55$, for $t = 0, \ldots, 5.2$, in increments of 0.1.

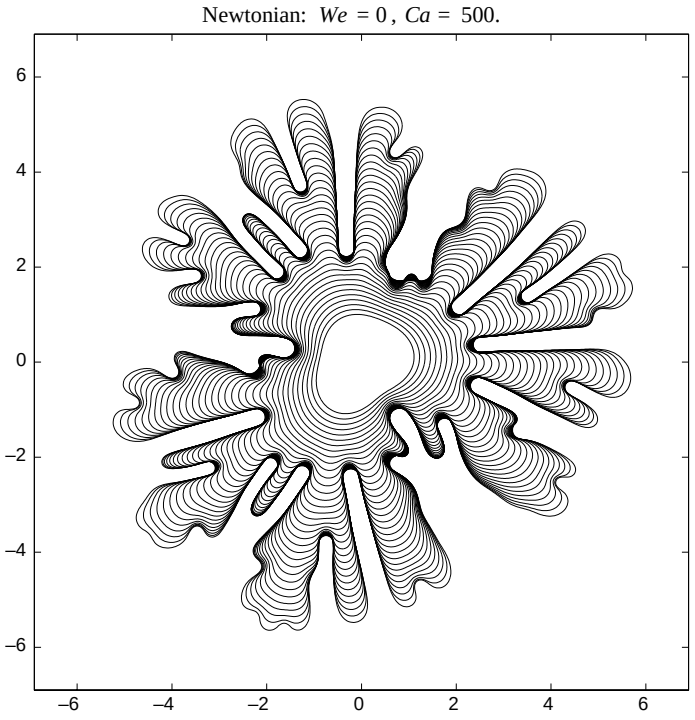

Fig. 14. Newtonian viscous fingering simulation for $Ca = 500$ at computational times $t = 0, \ldots, 3.4$, in increments of 0.1. Note that the scaling of the plot differs from Fig. 13.

summarized in Table 4. The maximum resolution used in our simulations is 4096 points along the interface and 632,691 unknowns in the pressure equation. The time-step is in the range $\Delta t = 0.5 \times 10^{-3}, \ldots, 2 \times 10^{-3}$ in all cases considered here.

Fig. 12 shows the evolution of an interface expanding into a a Newtonian fluid at $Ca = 250$. The resulting fingering pattern is of tip-splitting type, and in qualitative agreement with experiment [30]. (We note that even more developed patterns have been computed using boundary integral methods [21].)

The bubble evolution over long times in a weakly non-Newtonian fluid can differ significantly from the Newtonian case, as is illustrated by Fig. 13. The shear-thinning effect has reduced the number of tip-splittings, and yields fingers that are narrower than those formed in the Newtonian case. In some fingers one can see interface shapes reminiscent of side-branching, which is a non-Newtonian characteristic that has been observed in previous studies [16].

In Figs. 14 and 15, we consider simulations with a relatively small surface tension $Ca = 500$. Note that the scale in these figures differs from that used in Figs. 12–15.

The resulting fingering pattern for $We = 0$ (Fig. 14) has a strongly Newtonian character, with several tip-splittings, finger competition, and a relatively isotropic pattern at the final time $t = 3.4$. For $We = 0.55$ (Fig. 15), we see some non-splitting fingers, which have a distinctly non-Newtonian character. The initial tri-modal structure is still clearly visible in the non-Newtonian case at the final time, unlike in the Newtonian case. Several side-branched fingers can be seen, which is a non-Newtonian characteristic indicating a tip-splitting event that has been stopped by the shear-thinning effect.

Similar flows have been computed previously [16,25]. The fluid interface here, in Figs. 14 and 15, has developed far more structure than in the simulations with strongly shear thinning fluids using a lesser number of points along the interface. Further, no symmetries have been imposed.

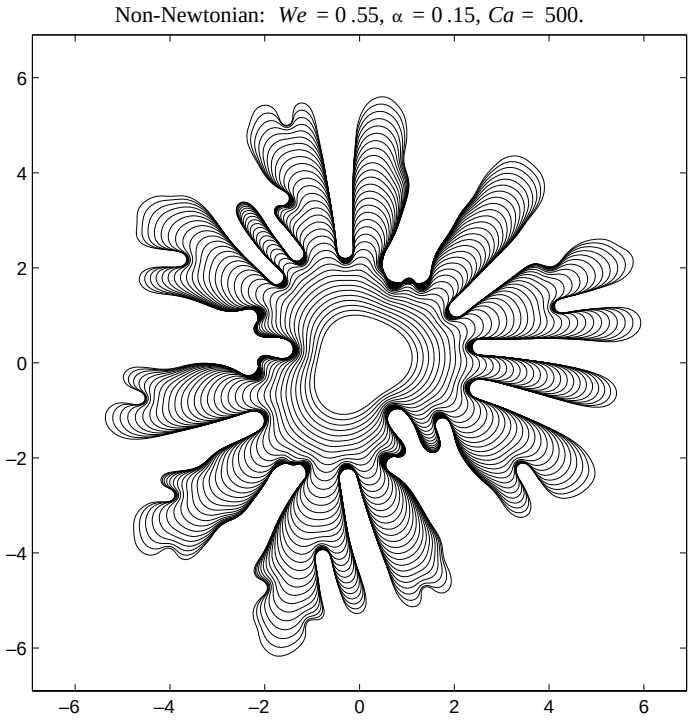

Fig. 15. Top: The expanding air/fluid interface in a moving overset grid simulation of non-Newtonian Hele–Shaw flow at $Ca = 500$, $We = 0.55$ at computational times $t = 0, \ldots, 3.4$, in increments of 0.1.

Table 4
The size of the component grids used in the discretization of the fluid domain for m points on the interface

m	Body fitted grid	Cartesian grid	Outer grid	Total
512	512×11	480×480	60×600	272,032
1024	1024×11	705×705	85×1066	598,899
2048	2048×11	705×705	85×1066	610,163
4096	4096×11	705×705	85×1066	632,691

The *Total* lists the total number of unknowns in the discretization of the pressure equation, and includes also ghostpoints and interpolation conditions.

In Fig. 15 we show close-ups of the moving overset grids near a splitting finger, at times $t = 2.4$, $t = 2.9$ and $t = 3.4$. The component grids are generated automatically, and adapt to the shape of the evolving air/fluid interface.

An intuitive understanding of the source of reduced tip-splittings can be gained by studying the viscosity field: Fig. 3 shows the weakly non-Newtonian viscosity (7) in the fluid external to the bubble at the final time $t = 3.4$ in Fig. 15. We see that the lowest viscosity occurs at the ends of the petals, and that the viscosity increases as one moves away from the tips.

It is this phenomena that results in the narrowed petals observed from the non-linear development of the Saffman–Taylor instability: the fluid velocity is locally accentuated by the non-Newtonian effect, which pulls the interface outwards at the tips. Thus, a tip remains a tip, and thereby the conditions for a lower local viscosity are maintained. Of course, this effect is limited by capillarity, which seeks to lower the length

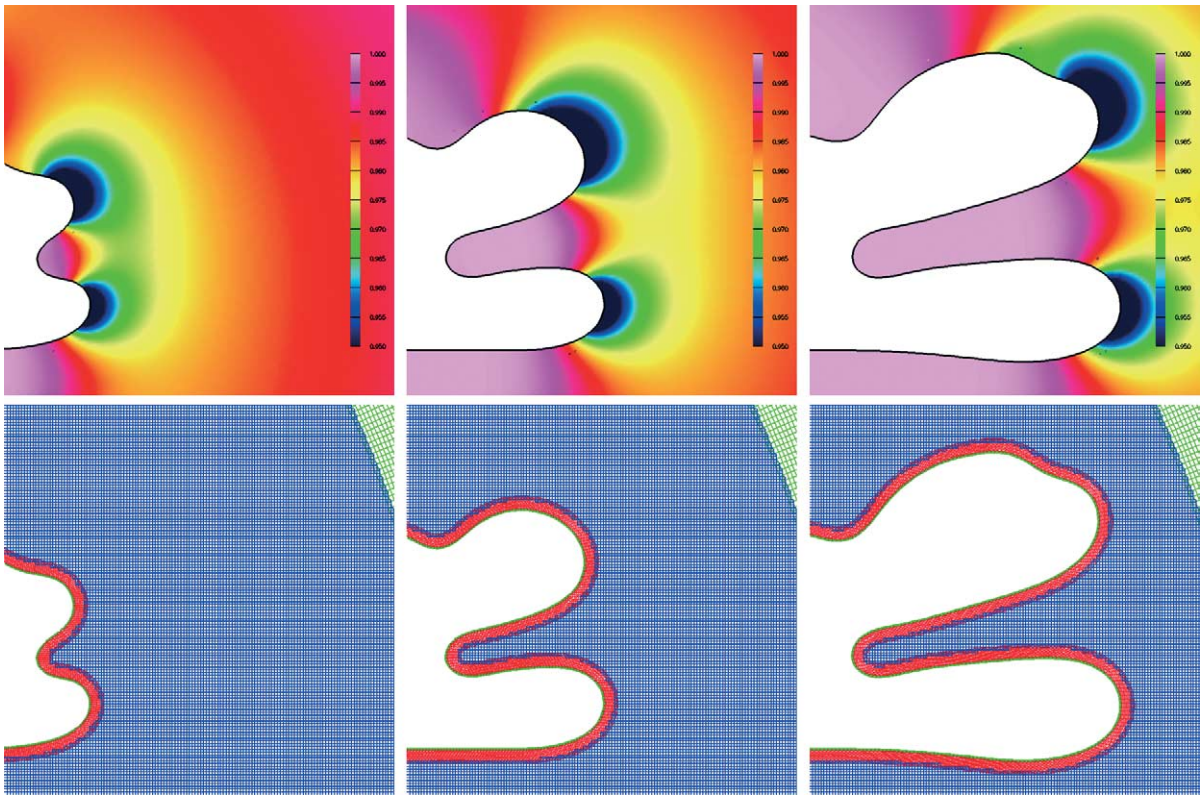

Fig. 16. A close-up of the computational grid used in Fig. 3, and the viscosity field, near the interface at times $t = 2.4$, $t = 2.9$ and $t = 3.4$. Here $We = 0.55$, $\alpha = 0.15$ and $Ca = 500$ (see Figs. 3, 4 and 15).

to area ratio. We note that the viscosity in our weakly non-Newtonian computations varies only by 5%, from $\bar{\mu} = 1.0$ in the fjords to $\bar{\mu} = 0.95$ at the tips. This variation is sufficiently large to induce significant changes in the pattern formation process. In Fig. 16, we show a close-up of the viscosity field in Fig. 3 near the interface.

5. Conclusions

In this paper we have developed a moving overset grid method for simulating the dynamics of fluid interfaces. The key feature of this method is the use of a thin body fitted grid that conforms to the deforming time dependent boundary and is coupled to fixed Cartesian grids.

We have studied computationally the non-Newtonian Saffman–Taylor instability in a weakly shear-thinning limit. In the case of an expanding circular interface, second-order accuracy was demonstrated in the interface position. We have also demonstrated good agreement with linear theory, which is a key feature of linear instabilities such as the Saffman–Taylor problem [34]. The effect of grid alignment errors was quantified in test cases, and shown to be insignificant for the length of simulations considered here. Simulations of asymmetric interfacial bubbles agree with predictions of reduced tip-splittings and increased

side-branching in non-Newtonian Hele–Shaw flow suggested by earlier theoretical and computational studies [11,25,27].

Moreover, the present method is able to achieve highly ramified viscous fingering patterns that are beginning to approach the level of detail seen in spectrally accurate boundary integral computations [21]. Improved numerical approaches to evolving the interface efficiently, and especially accurately, will also allow a computation of non-Newtonian viscous fingering patterns in the strongly non-Newtonian case. Long-time simulations have been performed for Newtonian flows [21], but only for intermediate time-scales in strongly shear-thinning flows [25].

While the focus here is on shear-*thinning* fluids, it would also be of interest to simulate viscous fingering in shear-*thickening* fluids where the local viscosity is an increasing function of the shear-rate. In recent work, Constantin, Widom and Miranda [11] perform a weakly non-linear analysis of non-Newtonian viscous fingering, and find mode-coupling conditions that in the shear-thickening case suggest finger widening and enhanced tip-splitting of the interface. In the shear-thinning case, their analysis predicts a reduction of tip-splitting and increased side-branch formation, which supports the findings in this paper.

There is a wealth of fundamental questions to be answered on non-Newtonian Hele–Shaw flows. A central one is the effect of the elastic response of the fluid (see [27] and the references therein). The non-Newtonian Darcy's law captures the non-Newtonian response of the bulk fluid for moderate Weissenberg numbers, $We = \mathrm{O}(1)$. Fast [13] performed a matched asymptotic analysis of the flow near the meniscus where Darcy's law is not valid, and derived non-Newtonian corrections to the Young–Laplace boundary condition (8). The analysis [13] suggests that as We is increased, shear-thinning effects near the meniscus become important and should be included in the pressure boundary conditions (see, however, the discussion in [16]). At still higher Weissenberg numbers the bulk flow will continue to be described by Eq. (2) but elastic effects at the interface will become important: Boundary conditions for this case have not yet been developed. Finally, in the high Weissenberg number limit, elastic effects in the bulk will become important and a new model of thin gap flow is needed to capture the full viscoelastic response in the fluid in a quasi-two dimensional setting. In some cases boundary integral methods will be applicable to compute such flows, but in many cases grid based methods such as the one developed here will be necessary.

Many other moving interface problems of current interest in fluid dynamics can be studied with an extension of the ideas presented in this paper. In recent work, Zhang et al. [38] considered experimentally the dynamics of an elastic filament pinned at its leading edge in a quasi-two dimensional soap-film flow. The flow interacts with the moving filament, generating vorticity that is shed at its freely moving end. The vorticity organizes itself into a structure reminiscent of a von Karman vortex street superimposed on a large scale traveling wave shape reflecting the flapping of the filament. One of us (P.F.) has been investigating a moving overset grid method that will resolve the multiple length scales present in the vorticity structure and perhaps capture the dynamics of this intriguing dynamic boundary flow. Preliminary results are available in Fast and Henshaw [14].

Acknowledgements

We thank Bill Henshaw for many useful suggestions on overset grid methods. Thanks to Peter Brown for suggesting the preconditioning scheme in Section 3.2. We thank Marsha Berger, Katarzyna Bernacki, Leslie Greengard, Lou Kondic, Brian Miller, Peter Palffy-Muhoray, and Don Schwendeman for discussions. This work was supported in part by NSF Grants DMS-9404554 and DMS-9396403, and DOE grant DE-FG02-88ER25053. A part of this work was performed under the auspices of the US Department of Energy by Lawrence Livermore National Laboratory under Contract No. W-7495-Eng-48.

Appendix A. The θ–L formulation

To control the stiffness of the time-evolution problem, we reformulate the motion of the interface in terms of the tangent angle $\theta(\beta,t)$ and arclength s_β. For completeness, we derive here the equations of motion in the θ–s_β frame, as in [21,36].

Let the interface be given by the closed curve $\mathbf{x}(\beta,t)$, where $\beta \in [0,2\pi]$ is the parametrization and t is time. Let $\mathbf{s}$ be the tangent vector to the curve, and $\mathbf{n}$ the inward pointing normal vector. The evolution of the interface is described by

$$\mathbf{x}_t = U\mathbf{n} + T\mathbf{s}, \tag{A.1}$$

where U is the normal velocity that describes the physics of the problem. The tangential velocity T has no physical meaning, and is specified later.

The tangent angle θ is related to the curve $\mathbf{x}$ through

$$x_\beta(\beta,t) = s_\beta(\beta,t)\cos\theta(\beta,t), \quad y_\beta(\beta,t) = s_\beta(\beta,t)\sin\theta(\beta,t).$$

The Frènet formulas $\partial_s\mathbf{s} = \kappa\mathbf{n}$, $\partial_s\mathbf{n} = -\kappa\mathbf{s}$ can be used to express the curvature as

$$\kappa = \theta_s. \tag{A.2}$$

The θ–s_β equations are found by taking a β derivative of Eq. (A.1) and using the Frénet formulas

$$\partial_t\partial_\beta\mathbf{x}(\beta,t) = \partial_t\{s_\beta(\cos\theta(\beta,t),\sin\theta(\beta,t))\} = U_\beta\mathbf{n} + T_\beta\mathbf{s} + U(-s_\beta\kappa\mathbf{s}) + T(s_\beta\kappa\mathbf{n}),$$

and hence θ and s_β satisfy

$$\partial_t s_\beta = T_\beta - \theta_\beta U, \tag{A.3}$$

$$\partial_t\theta = \frac{1}{s_\beta}\{U_\beta + T\theta_\beta\}. \tag{A.4}$$

Appendix B. Algorithm for body fitted grid generation

In this section, we discuss the details of generating the body fitted grid using Eq. (16). The use of this equation for grid generation is discussed by Sethian [35].

We solve the body fitted grid generation Eq. (16) using the θ–L formulation

$$\frac{\partial\theta}{\partial\xi}(\eta,\xi) = \frac{2\pi}{L(\xi)}\left(\frac{\partial U}{\partial\xi} + T\frac{\partial\theta}{\partial\eta}\right), \tag{B.1}$$

$$\frac{\partial L}{\partial\xi}(\eta,\xi) = -\int_0^{2\pi}\frac{\partial\theta}{\partial\eta'}(\eta',\xi)U(\eta',\xi)\mathrm{d}\eta', \tag{B.2}$$

where

$$U(\eta,\xi) = -1 + C\kappa(\eta,\xi) = -1 + C\frac{2\pi}{L(\xi)}\frac{\partial\theta}{\partial\eta}(\eta,\xi) \tag{B.3}$$

and

$$T(\eta,\xi) = \int_0^{\eta} \frac{\partial\theta}{\partial\eta'}(\eta',\xi)U(\eta',\xi)\mathrm{d}\eta' - \frac{\eta}{2\pi}\int_0^{2\pi} \frac{\partial\theta}{\partial\eta'}(\eta',\xi)U(\eta',\xi)\mathrm{d}\eta'. \tag{B.4}$$

Here C is a small parameter. The initial data at $\xi = 0$ is given by the fluid interface Γ. Eqs. (B.1)–(B.4) are solved in Fourier space in η using a second-order accurate integrating factor Adams–Bashforth method to discretize the time-like variable ξ (see Section 3.3).

Remark. The 'grid generation equation' (16) is completely separate from the equations of motion for the fluid interface. The only purpose of solving this equation at a given time is to generate a body fitted grid. Any other approach that produces a body fitted grid near the fluid interface could be used just as well.

References

[1] R.F. Almgren, W.-S. Dai, V. Hakim, Scaling behavior in anisotropic Hele–Shaw flow, Phys. Rev. Lett. 71 (1993) 3461–3464.
[2] Satish Balay, William D. Gropp, Lois Curfman McInnes, Barry F. Smith. PETSc 2.0 users manual, Technical Report ANL-95/11 – Revision 2.0.24, Argonne National Laboratory, 1999.
[3] M. Ben Amar, Exact self-similar shapes in viscous fingering, Phys. Rev. A 43 (1991) 5724.
[4] R.B. Bird, R.C. Armstrong, O. Hassager, Dynamics of Polymeric Liquids, Wiley, New York, 1987.
[5] J.O'M. Bockris, A.K.N. Reddy, Modern Electrochemistry, Plenum Press, New York, 1970.
[6] D.L. Brown, W.D. Henshaw, and D.J. Quinlan, Overture: an object oriented framework for solving partial differential equations, in: Scientific Computing in Object-Oriented Parallel Environments, Springer Lecture Notes in Computer Science, vol. 1343, 1997.
[7] A. Buka, J. Kertesz, T. Viscek, Nature 323 (1986) 424.
[8] A. Buka, P. Palffy-Muhoray, Z. Racz, Viscous fingering in liquid crystals, Phys. Rev. A 36 (1987) 3984.
[9] W.M. Chan, Hyperbolic methods for surface and field grid generation, in: J.F. Thompson, B.K. Soni, N.P. Weatherill (Eds.), Handbook of Grid Generation, CRC Press, Boca Raton, 1999 (Chapter 5).
[10] G. Chesshire, W.D. Henshaw, Composite overlapping meshes for the solution of partial differential equations, J. Comput. Phys. 90 (1990) 1.
[11] M. Constantin, M. Widom, J.A. Miranda, Mode-coupling approach to non-Newtonian Hele–Shaw flows, Phys. Rev. E 67 (2003) 026313.
[12] H. Van Damme, E. Lemaire, Non-Newtonian fingering and visco-elastic fracturing, in: J.C. Charmet, S. Roux, E. Guyon (Eds.), Disorder and Fracture, Plenum Press, New York, 1990, p. 83.
[13] P. Fast, Interfacial conditions for shear-thinning Hele–Shaw flow, J. Non-Newtonian Fluid Mech., submitted, available as LLNL Tech. Rep. UCRL-JC-149 667, 2002.
[14] P. Fast, W.D. Henshaw, Time accurate simulation of viscous flow around deforming bodies using overset grids, AIAA paper 2001–2604, 2001.
[15] P. Fast and W.D. Henshaw, Oges user guide, version 2: a solver for steady state boundary value problems on overlapping grids. Research Report UCRL-MA-132234, Lawrence Livermore National Laboratory, 2002.
[16] P. Fast, L. Kondic, M.J. Shelley, P. Palffy-Muhoray, Pattern formation in non-Newtonian Hele–Shaw flow, Phys. Fluids 13 (2001) 1191–1212.
[17] B. Fornberg, A Practical Guide to Pseudospectral Methods, Cambridge University Press, Cambridge, UK, 1996.
[18] W.D. Henshaw, A fourth-order accurate method for the incompressible Navier–Stokes equations on overlapping grids, J. Comput. Phys. (1994) 13–25.
[19] W.D. Henshaw, Ogen: the Overture overlapping grid generator, Technical Report UCRL-MA-132237, Lawrence Livermore National Laboratory, 2002.
[20] G.M. Homsy, Viscous fingering in porous media, Ann. Rev. Fluid Mech. 19 (1987) 271.
[21] T. Hou, J. Lowengrub, M.J. Shelley, Removing the stiffness from interfacial flow with surface-tension, J. Comput. Phys. 114 (1994) 312.
[22] T. Hou, J. Lowengrub, M.J. Shelley, Boundary integral methods for multicomponent fluids and multiphase materials, J. Comput. Phys. 169 (2001) 302.
[23] T.Y. Hou, Z. Li, S. Osher, H. Zhao, A hybrid method for moving interface problems with application to the Hele–Shaw flow, J. Comput. Phys. 134 (2) (1997) 236–252.
[24] L. Kondic, P. Palffy-Muhoray, M.J. Shelley, Models of non-Newtonian Hele–Shaw flow, Phys. Rev. E 54 (1996) 4536.
[25] L. Kondic, M.J. Shelley, P. Palffy-Muhoray, Non-Newtonian Hele–Shaw flow and the Saffman–Taylor instability, Phys. Rev. Lett. 80 (1998) 1433.

[26] J.S. Langer, in: H.E. Stanley (Ed.), Statistical Physics, North-Holland, Amsterdam, 1986.
[27] A. Lindner, D. Bonn, E.-C. Poire, M. Ben Amar, J. Meunier, Viscous fingering in non-newtonian fluids, J. Fluid Mech. 469 (2002) 237.
[28] R.L. Meakin, Composite overset structured grids, in: J.F. Thompson, B.K. Soni, N.P. Weatherill (Eds.), Handbook of Grid Generation, CRC Press, Boca Raton, 1999 (Chapter 11).
[29] S.S. Park, D.J. Durian, Viscous and elastic fingering instabilities in foam, Phys. Rev. Lett. 72 (1994) 3347.
[30] L. Paterson, Radial fingering in a Hele–Shaw cell, J. Fluid Mech. 113 (1981) 513.
[31] E.C. Poiré, M. Ben Amar, Finger behavior of a shear thinning fluid in a Hele–Shaw cell, Phys. Rev. Lett. 81 (1998) 2048–2051.
[32] J.S. Ro, G.M. Homsy, Viscoelastic free surface flows: thin film hydrodynamics of Hele–Shaw and dip coating flows, J. Non-Newtonian Fluid Mech. 57 (1995) 203–225.
[33] Y. Saad, Iterative methods for Sparse Linear Systems, PWS Publishing, New York, 1996.
[34] P.G. Saffman, G.I. Taylor, The penetration of a fluid into a porous medium or Hele–Shaw cell containing a more viscous liquid, Proc. Roy. Soc. London., Ser. A 245 (1958) 312.
[35] J. Sethian, Level Set Methods, Cambridge University Press, New York, 1996.
[36] J. Strain, A boundary integral approach to unstable solidification, J. Comput. Phys. 85 (1989) 342.
[37] Y. Tu, Saffman–Taylor problem in sector geometry: solution and selection, Phys. Rev. A 44 (1991) 1203.
[38] J. Zhang, S. Childress, A. Libchaber, M.J. Shelley, Flexible filaments in a flowing soap film as a model for one-dimensional flags in a two-dimensional wind, Nature 408 (2000) 835–839.
[39] H. Zhao, J.V. Maher, Viscoelastic effects in patterns between miscible liquids, Phys. Rev. A 45 (1992) 8328.
[40] H. Zhao, J.V. Maher, Associating-polymer effects in a Hele–Shaw experiment, Phys. Rev. E 47 (1993) 4278.